

Creep features and mechanism of active-layer detachment slide on the Qinghai-Tibet Plateau by InSAR

Fei Wang^{a,b}, Zhi Wen^{a,*}, Qiang Gao^a, Qihao Yu^a, Desheng Li^c, Liangzhi Chen^d

^a State Key Laboratory of Frozen Soil Engineering, Northwest Institute of Eco-Environment and Resources, Chinese Academy of Sciences, Lanzhou 730000, China

^b University of Chinese Academy of Sciences, Beijing 100049, China

^c Nanjing University of Science and Technology School of Science, Nanjing 210000, China

^d Swiss Federal Institute for Forest, Snow and Landscape Research WSL, Zürcherstrasse 111 CH-8903, Birmensdorf 8903, Switzerland

ARTICLE INFO

Keywords:

Active-layer detachment slide

InSAR

Qinghai-Tibet Plateau

Creep feature

ABSTRACT

An active-layer detachment slide (ALDS) occurred on September 21, 2018, in the Fenghuoshan mountains of the Qinghai-Tibet Plateau (QTP) (34°39.1'N, 92°53.5'E). With the Sentinel-1A image from Copernicus Open Access Hub, we use small baseline subset to achieve the time series deformation map to analyze the thermo-spatial creep feature, motion pattern, trigger mechanism, and correlation of environmental changes in the ALDS. The SBAS (the Small Baselines Subset) results show that the trailing part of ALDS has the largest downward deformation rate; however, the leading area was small, and the creep feature shows a clear seasonal change corresponding to the freeze-thaw cycle. We also divide the motion pattern into three stages: moderate creep, steady creep, and rapid collapse, based on the deformation rate. Meteorological observation and reanalysis data, as well as borehole data, show that heavy precipitation in the summer of 2017 and 2018 promote the formation of underground ice, while high air temperatures allow the thaw plane to reach the ice-rich zone, and confined water generated by the two-way freezing process result in ALDS. Moreover, there exists a temporal delay of approximately one month in the association between deformation rate and both precipitation and temperature. Furthermore, there is a clear correlation between variations in thawing depth and deformation, which serves as the primary catalyst for ALDS in permafrost regions. Finally, we also identify that ALDS is a mixed-type landslide and that cumulative deformation and creep damage play the main roles in triggering ALDS.

1. Introduction

Large-scale traditional energy consumption and the greenhouse effect caused by human activities have contributed to global warming (Guo et al., 2023; Yu et al., 2023). The permafrost has been degrading rapidly under a warming climate (Nelson et al., 2001; Ma et al., 2006; Schaefer et al., 2011; Niu et al., 2016; Liljedahl et al., 2016; Chadburn et al., 2017; Peng et al., 2018). Numerous thermokarst features, including active layer detachment slides, retrogressive thaw slumps, and thermokarst lakes, have been discovered and extensively documented in permafrost regions worldwide (Lewkowicz, 2010; Zwieback et al., 2017; Niu et al., 2012, 2016; Luo et al., 2019; Li et al., 2019). QTP is one of the most climatic sensitive places in the global and the regional climate features with the amplification of global warming (Wu et al., 2013; Ran et al., 2018; Song et al., 2014; Sun et al., 2015). Recently, rising air temperatures and precipitation on the QTP have led to an increase in

slope failures which may endanger buildings and engineering structures such as the Qinghai-Tibet railway, Qinghai-Tibet highway and other projects, significantly endangering the lives and property lives and property (Niu et al., 2016; Luo et al., 2019; Li et al., 2019; Guo et al., 2021; Jiang et al., 2022).

The phenomenon known as ALDS refers to a type of shallow landslide that occurs within permafrost environments (Lewkowicz and Harris, 2005a, 2005b). This event is characterized by the downward movement of the active layer, which slides over the underlying permafrost layer. It is most prevalent in ice-rich environments (Niu et al., 2016; Jiang et al., 2022). High temperatures and heavy precipitation in the summer are usually responsible for their development on slopes that are relatively gentle (Jorgenson and Osterkamp, 2005; Kokelj et al., 2013; Niu et al., 2016; Jiang et al., 2022). The ALDS in permafrost is different from slope failure in general areas due to the exceptional structural geological features of freezing soil, which normally occurs following the

* Correspondence author.

E-mail address: wenzhi@lzb.ac.cn (Z. Wen).

<https://doi.org/10.1016/j.catena.2023.107782>

Received 23 July 2023; Received in revised form 7 December 2023; Accepted 23 December 2023

Available online 4 January 2024

0341-8162/© 2023 The Authors. Published by Elsevier B.V. This is an open access article under the CC BY-NC-ND license (<http://creativecommons.org/licenses/by-nc-nd/4.0/>).

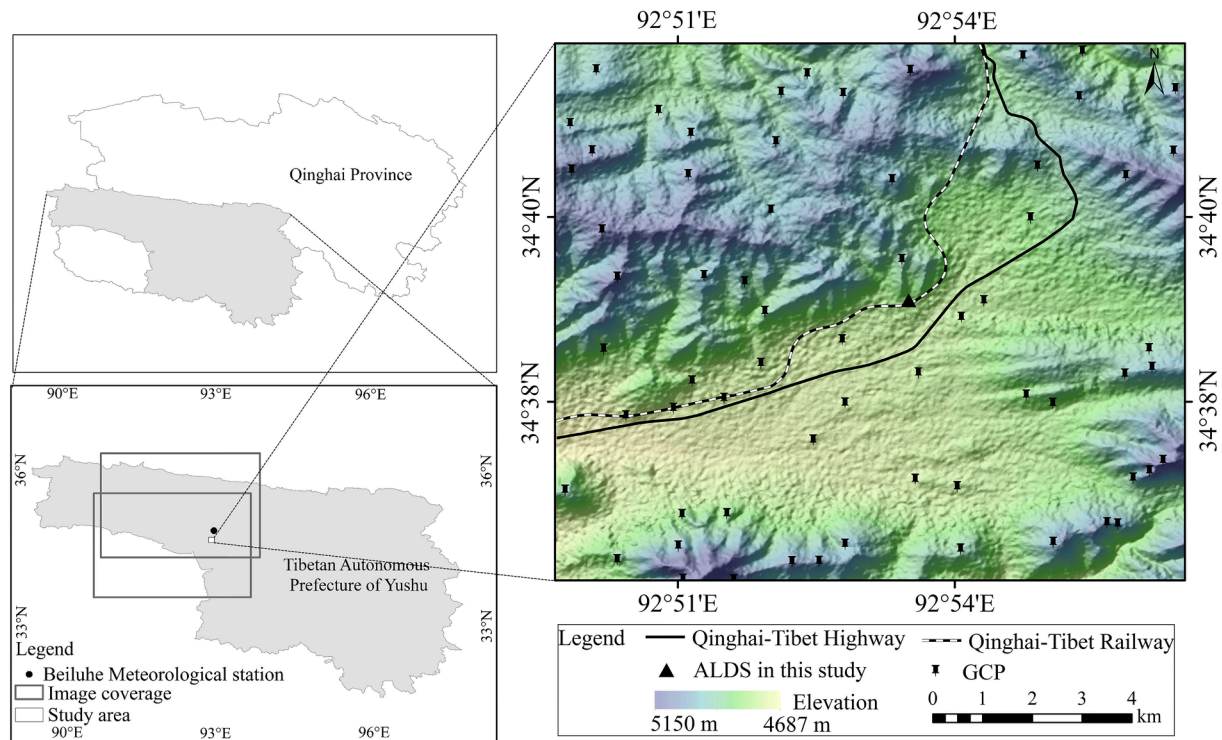


Fig. 1. Location of the study area and site of ALDS in the Fenghuoshan mountain. GCPs are the ground control points used in SBAS method to refine orbits and calculate phase offset.

underground ice surface or freeze-thaw surface (McRoberts and Morgenstern, 1974; Lewkowicz and Way, 2019; Costard et al., 2021; Niu et al., 2016; Yin et al., 2021). The creep characteristics of the landslides in permafrost regions are remarkable because of the rheology of the frozen soil. The ice-rich frozen slope will creep downward, and long-term creep is inevitable to cause active-layer detachment slides (Niu et al., 2016; Kokelj et al., 2013; Sun et al., 2017; Jiang et al., 2022). Nevertheless, the recording of the long-term creep process of individual landslide sections is seldom applied due to the constraints of conventional landslide monitoring applications.

InSAR, an effective approach, is employed for investigating land surface displacements with great precision (Massonnet and Feigl, 1998; Berardino et al., 2002). When comparing with conventional methods such as Global Navigation Satellite System (GNSS) and optical remote sensing, InSAR stands out as a highly accurate and widely encompassing method for monitoring and detecting landslides that move slowly. Its effectiveness is attributed to its extensive spatial coverage and ability to acquire data over long periods regardless of weather conditions (Cigna et al., 2014; Wasowski and Bovenga, 2014; Zhang et al., 2016; Calvello et al., 2017). The capacity to identify instances of rapid landslide deformation and examine correlations with a variety of triggers is an additional advantage that may be gained from analyzing displacement time series that are provided by InSAR (Li et al., 2020). The InSAR algorithms effectively mitigate and rectify the spatial-temporal decorrelations and atmospheric delays (Ferretti et al., 2001; Berardino et al., 2002; Hooper et al., 2004; Ferretti et al., 2011) and have been frequently employed in identifying potential landslide and measure landslide surface deformation (Wasowski and Bovenga, 2014; Novellino et al., 2017; Zhang et al., 2018; Ambrosi et al., 2018; Li et al., 2020). In recent years, the application of InSAR technique for the detection of surface deformation and thermokarst landslides has been increasingly utilized in permafrost environments (Chen et al., 2012; Zhao et al., 2016; Zhang et al., 2019; Hao et al., 2019). Nonetheless, previous studies primarily concentrated on the utilization of the InSAR technique for the detection and analysis of permafrost surface deformation (Zhang et al., 2019), and

limited studies integrate time-series of InSAR to examine the peculiarities of slope creep and its primary trigger in permafrost regions.

In this study, we first described a representative ALDS that occurred in the Fenghuoshan Mountains on September 21, 2018. We used freely available SAR data (Sentinel-1A) between 2014 and 2018 to identify and monitor ALDS in the Fenghuoshan Mountains, Qinghai-Tibet Plateau. After that, the SBAS method was utilized to extract the creep process of the ALDS in the Fenghuoshan Mountains. This method is applicable in both rural and urban regions (Wasowski et al., 2014; Reyes-Carmona et al., 2020). We also analyzed the spatial-thermal feature of the slope creep, and investigated the relations between creep and precipitation, air and ground surface temperature, and the hydro-thermal dynamic process of the active layer. Finally, we revealed the major triggers and developing mechanisms of the ALDS.

2. Study area and data

2.1. Study area

The study site is located in the Fenghuoshan Mountains (Fig. 1), characterized by an elevation range of 4612 m.a.s.l to 5300 m.a.s.l, and an average elevation of around 4700 m.a.s.l (Jiang et al., 2022). January is the coldest month, with monthly average temperature about -15°C , while July and August are the warmest, with monthly average temperature reaching about 9°C and mean annual air temperatures (MAAT) ranging from -5.0 to -6.0°C (Luo et al., 2019). Annual precipitation in the region fluctuates between 300 and 400 mm, with the majority of precipitation falling between June and September. Observed data from the Fenghuoshan Mountain Permafrost Observational Station which is located 9 km north of the ALDS site, shows that summer precipitation in the region significantly increased from 2004 to 2018, significantly from 2006 to 2018 (Jiang et al., 2022). The main type of plant found in the study region is alpine grassland. According to the findings of Jiang et al., 2022, the investigated region exhibits a range of active layer thickness (ALT) values spanning from 0.7 to 3.6 m, along with a mean annual

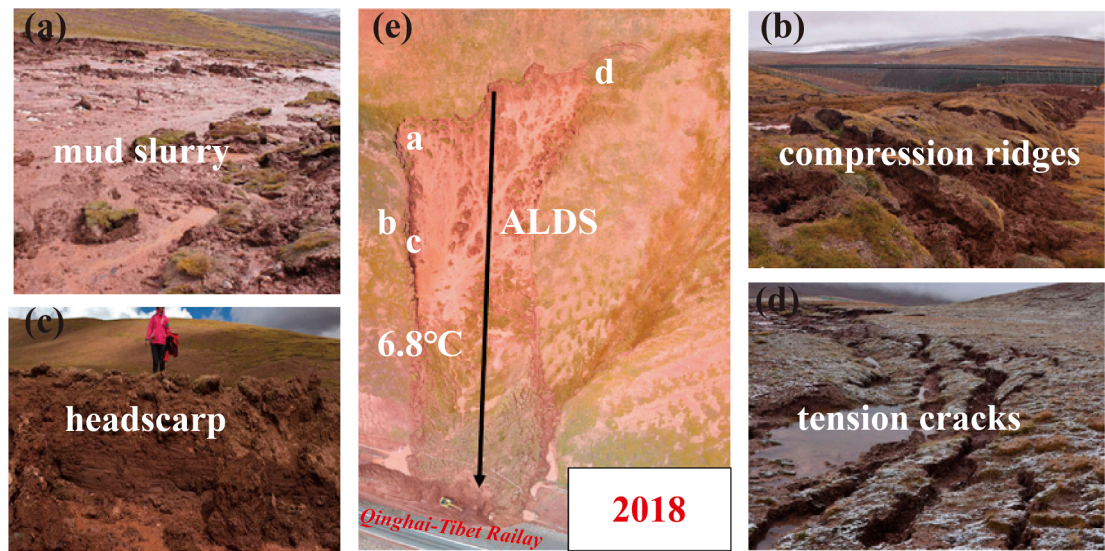


Fig. 2. Pictures of ALDS (Referenced from Jiang et al., 2022). (a) mud slurry. (b) compression ridges. (c) head scarp. (d) tension cracks. (e) ALDS.

Table 1
Detailed parameters of Sentinel-1A data.

Parameter	Value
Orbit direction	Ascending
Microwave band	C-band
polarization	VV
Repeat cycle	12 d
Incidence angle	39.8°
Resolution (slant range, azimuth)	2.3 × 13.9 m
Temporal coverage	October 2014 to September 2018
Number of frames	84

ground temperature (MAGT) ranging between 0.4 and 3.6 °C. The region’s permafrost is characterized by an abundant volume ice content, with 70 % of it containing over 30 % ice and 20 % having more than 50 %. The thickness of the permafrost in this region varies from 20 to 80 m (Niu et al., 2016; Luo et al., 2019).

2.2. ALDS in Fenghuoshan Mountains

On September 21, 2018, ALDS occurred in Fenghuoshan Mountain and posed a direct threat to the Qinghai Tibet Railway (Fig. 2). The results of the study survey reveal that the ALDS is 145 m in length and 46 m in width, and the head scarp is 2.2–2.5 m high (Fig. 2d). The upslope of the non-sliding zone behind the head scarp is fracture fractures flowing parallel to the scarp (Fig. 2c). The slope gradient varies between 4.8 and 9.0°, with an average gradient of 6.8° (Fig. 2e). In line with the finding of previous studies, landslides in permafrost tend to occur on moderate slopes (Ma et al., 2006; Niu et al., 2016; Luo et al., 2019). Based on the borehole information provided by Jiang et al., 2022, the active layer measures approximately 2.4 m in depth, with the freeze-thaw interface primarily consisting of clay and silty clay textures. Moreover, it is worth noting that underground harbors a considerable amount of solidified water, extending from the lower boundary of the active layer to at least depth of 5 m (Jiang et al., 2022).

2.3. Data

2.3.1. Satellite SAR and ancillary data

Given the scarcity of available descending images, we have opted to utilize ascending C-band SAR data obtained from the Sentinel-1 A satellite during the period spanning from January 2014 to September 2018. Table 1 shows the primary parameters of the Sentinel 1A. Additionally,

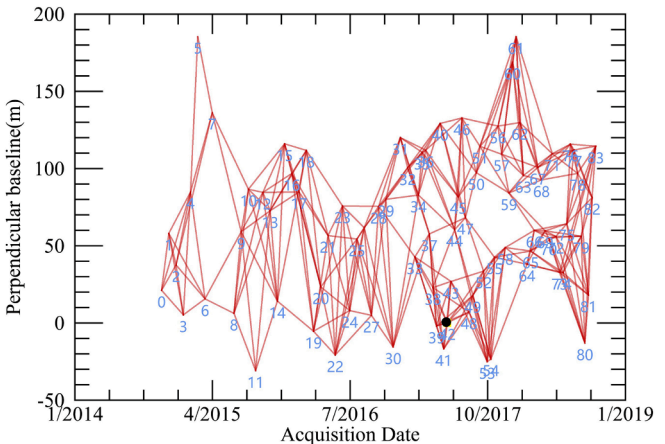


Fig. 3. Spatiotemporal baselines of interferograms. We removed interferograms with low coherence and heavy unwrapping error. The black plot is the super master image.

precision orbit determination (with an accuracy of less than 5 cm) was collected in the InSAR processing for orbit error correction (Zheng et al.,2022). The SAR data and precision orbit determination were downloaded in the EARTHDATA (<https://search.asf.alaska.edu/>). The Shuttle Radar Topography Mission (SRTM) digital elevation model, which was obtained in the Geospatial Data Cloud (<https://www.gscloud.cn/>) was utilized for the estimation and elimination of the topographic phase. Fig. 3 displays the combination of 325 final

Table 2
Detailed parameters of meteorological data and reanalysis data.

Data source	Variables
Meteorological data	Air temperature (sensor model is HMP45C, accuracy ±0.1 °C, from 2015 to 2018) Precipitation (sensor model is t-200b, accuracy ±1 %, from 2015 to 2018) Soil water content (accuracy ±0.03, from 2015 to 2018) Soil temperature of the borehole (from 2015 to 2018, at the depths of 0.5, 1.0, 1.5, 2.0, 2.5, 3.0, 3.5, 4.0, 4.5, 5.0 m)
Reanalysis data	Ground surface temperature (with a resolution of 1 km, from 2015 to 2018) Precipitation (with a resolution of 1 km, from 2015 to 2018)

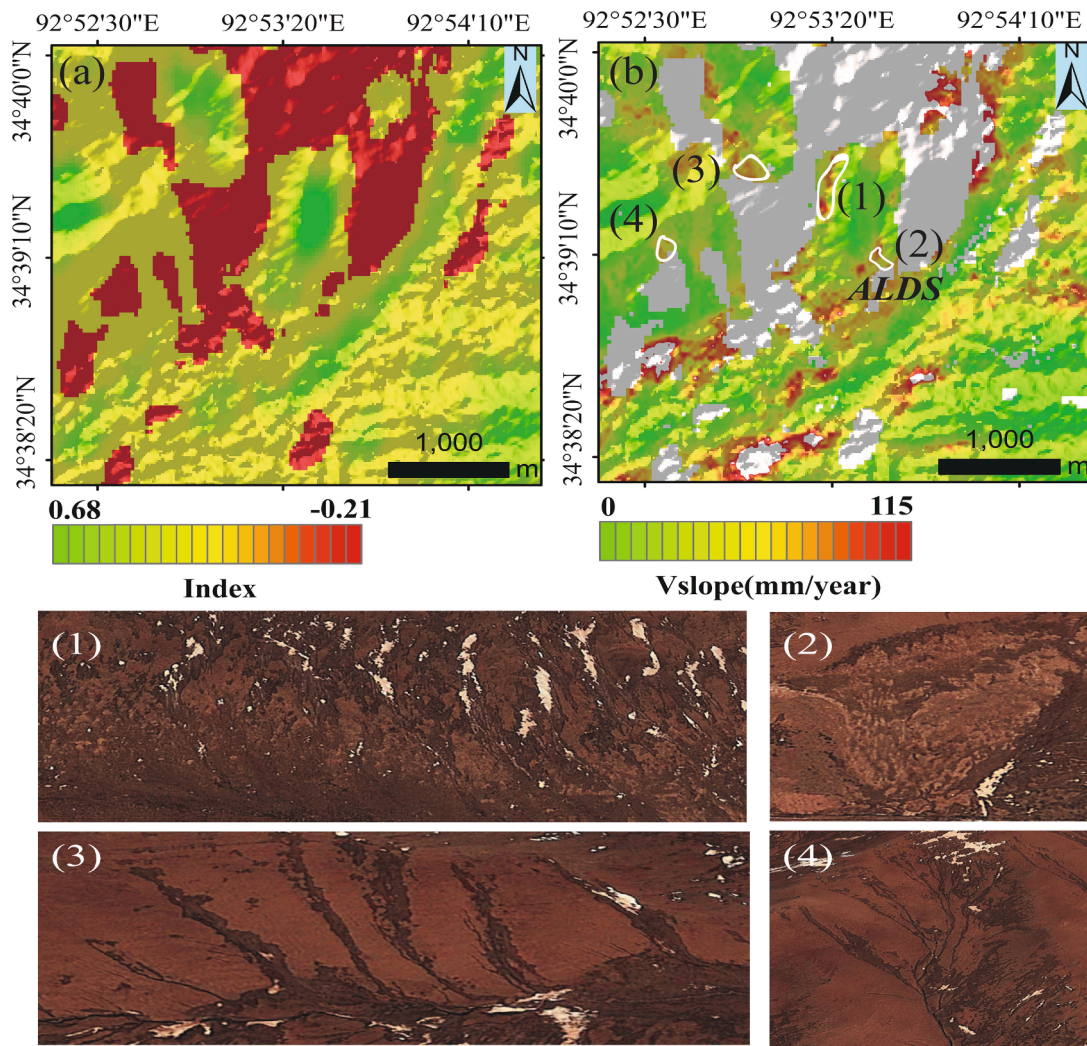


Fig. 4. The conversion index and downslope deformation rate map. (a) Conversion index. (b) Deformation rate of downslope direction in the study area. (1), (2), (3) and (4) are the images achieved in Google Earth, and the annual average downslope creep rates are -80 , -70 , -65 , and -55 mm/year, respectively.

interferograms for SBAS analyses, generated by merging images of Sentinel-1A with temporal baselines (≤ 120 d) and max spatial baseline (≤ 160 m). Lastly, we acquired a Gaofen-2 optical remote sensing imagery (with a resolution of up to 0.8 m) for December 2019 (Fig. 5b) from the Natural Resources Satellite Services Platform (<https://www.sasclouds.com/>) to locate ALDS's slide boundary.

2.3.2. Meteorological data

We acquired observed meteorological data (Table 2) from Beiluhe weather station (Chen, 2018) and reanalyzed data (Table 2) from the National Tibetan Plateau Data Center (Zhou et al., 2021; Peng, 2019) to conduct an investigation into the creep characteristics and mechanism of the ALDS. Additionally, the soil temperature obtained from a borehole located 2 km away from the Beiluhe weather station was utilized in the subsequent analysis. Python was utilized to manage the reanalysis data, while thaw depths were determined by employing linear interpolation to estimate daily soil temperatures within the range of 0°C .

3. Method

3.1. SBAS time series analysis

We processed the Sentinel-1A data with the multi-look factor of 1 in azimuth and 4 in range to reduce pixelated noise (Gong et al., 2019). The

Goldstein filtering method was employed in our study, where we established a minimum signal-to-noise threshold (SNR) value. This approach effectively enhanced the visibility of fringes and mitigated the noise caused by temporal or baseline-related decorrelation (Goldstein and Werner, 1998; Baran et al., 2003). We chose the CTs (coherence points) with coherence larger than 0.4 to phase unwrapping, and the correlation of corresponding pixels of the two SAR images should be calculated by Eq. (1). The Minimum Cost Flow algorithm was employed for unwrapping interferograms to address the ambiguity associated with the 2π phase wrapping (Pepe and Lanari, 2006). Eq. (2) could be used to estimate the unwrapped differential interferometric phase:

$$\gamma = \frac{E\{S_1 \cdot S_2^*\}}{\sqrt{E\{|S_1|^2\} \cdot E\{|S_2|^2\}}}$$
 (1)

where γ is correlation, which ranges from 0 to 1. $E\{\}$ Indicates averaging. S_1 is the corresponding pixels of the two SAR images. $*$ represents the conjugate multiplication.

$$\begin{aligned} \Delta\phi_i(x, y) &= \phi(t_2, x, y) - \phi(t_1, x, y) = \Delta\phi_{\text{disp}} + \Delta\phi_{\text{topo}} + \Delta\phi_{\text{atm}} + \Delta\phi_{\text{noise}} \\ &\approx \frac{4\pi}{\lambda} [d(t_2, x, y) - d(t_1, x, y)] + \frac{4\pi B_{\perp k}}{\lambda R \sin\theta} \Delta z + \frac{4\pi}{\lambda} [d_{\text{atm}}(t_2, x, y) - d_{\text{atm}}(t_1, x, y)] \end{aligned}$$
 (2)

where $\Delta\phi_i(x, y)$ is interferometric phase. $\phi(t_1, x, y)$ and $\phi(t_2, x, y)$ are

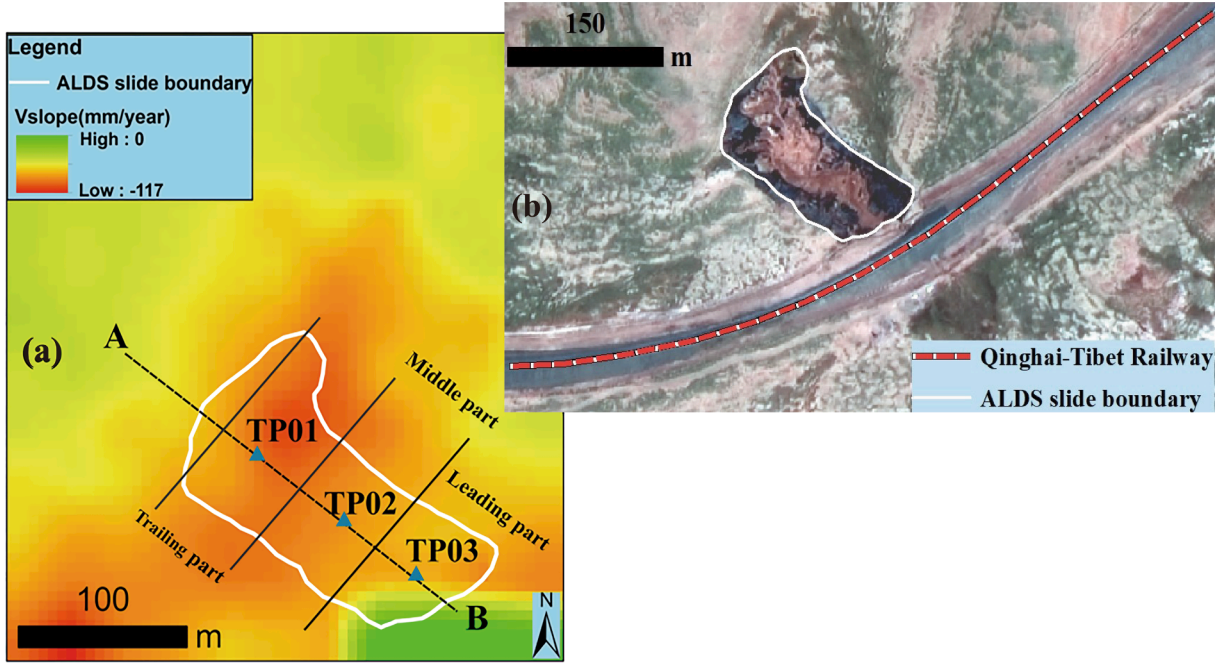


Fig. 5. Deformation rate of ALDS. (a) The average deformation rate in the downslope direction for ALDS. The dashed black line of AB denotes profile locations. The solid black lines divide the ALDS into three sections: the trailing part, the middle part, and the leading part. The blue triangle represents the time series point. (b) High-resolution satellite imagery of the region from Gaofen-2. The white line compasses the sliding area.

interferometric phases at moments t_1 and t_2 . λ is wavelength. θ is radar incident angle. $B_{\perp k}$ is the perpendicular baseline of interferograms. R denotes the distance from the ground target to the satellite. $\Delta\phi_{disp}$ is the deformation phase in the satellite's LOS (line of sight) direction. $\Delta\phi_{topo}$ is the phase contribution caused by the inaccuracy of the terrain data, which can be minimized using high-resolution digital elevation model (DEM) (Tong and David, 2016). In addition, we reduced the topography error by estimating the residual topography height. $\Delta\phi_{atm}$ denotes the atmospheric delay, comprising of ionospheric and tropospheric component (Gray et al., 2000). The ionospheric component is frequently observed in L-band SAR systems, whereas it is infrequently observed in C-band SAR systems (Fattah and Amelung, 2015). Hence, we do not consider an ionospheric delay. Eq. (3) can be used to estimate and separate the tropospheric component using a quadratic model (Xu et al., 2013). $\Delta\phi_{noise}$ consists of thermal noise, decorrelation noise, and other noises.

$$\beta(x, y) = a_0 + a_1x + a_2y + a_3xy + a_4x^2 + a_5y^2 + a_6\eta(x, y) \quad (3)$$

where β is the tropospheric delay, η is the elevation, a_i denotes unknown coefficients.

3.2. Transforming LOS measurements into the downward direction

The InSAR method normally detects the deformation of the LOS direction. We transformed LOS into downslope by considering the geometries of the satellites and the terrain parameters (slope, aspect) using Eq. (4) (Schlgel et al., 2015).

$$V_{slope} = \frac{V_{los}}{\varepsilon_{index}} \quad (4)$$

ε_{index} can be formulated as below (Eq. (5) (Notti et al., 2014).

$$\left\{ \begin{array}{l} \varepsilon_{index} = n_{los} \times n_{slope} \\ n_{los} = (-\sin\theta\cos\alpha, \sin\theta\sin\alpha, \cos\theta) \\ n_{slope} = (-\sin\beta\cos\varphi, -\cos\beta\cos\varphi, \sin\varphi) \\ \text{if } 0 < |\varepsilon_{index}| \leq 0.2, \varepsilon_{index} = 0.2, \text{ otherwise, } \varepsilon_{index} = \text{realvalue} \end{array} \right\} \quad (5)$$

where n_{los} is the unit vector in LOS direction, n_{slope} is the unit vector in downslope direction, θ and α are the incidence angle and the track angle respectively, β and φ represent the slope aspect and slope angle. The deformation rate conversion is dependent on converting index, as demonstrated by Eq. (5). Aspect and radar look vectors can be angled acutely or obtusely, so the conversion index factor can have a positive or negative value. However, when the conversion index approaches 0, the deformation rate down the slope approaches infinity (Schlgel et al., 2015). To avoid this situation, we replaced the value of the index greater than or equal to zero and less than 0.2 by 0.2 and the value of the index less than zero and greater than -0.2 by -0.2. Fig. 4 shows the conversion index and downslope deformation rate map.

3.3. Slope stability calculation

In the slope of the permafrost area, underground ice is generally used as an impermeable layer to make the seepage direction of groundwater above the upper limit approximately perpendicular to the ice surface (Niu et al., 2016). The slope safety factor of permafrost areas could be determined using the infinite slope model and the principle of effective stress, as shown in Eq. (6) (Niu et al., 2016):

$$F_s = \frac{c' + [(1-m)\gamma + m(\gamma_{sat} - \gamma_w)]z\cos^2\alpha\sin\psi'}{[(1-m)\gamma + m\gamma_{sat}]z\sin\alpha\cos\alpha} \quad (6)$$

where m is the ratio of height of the water table above the slip surface to the slip surface's depth, ψ' is the effective frictional angle ($^\circ$), γ is the weight of the soil located above the groundwater level (kN/m^3), γ_{sat} is the weight of saturated soil (kN/m^3), z is vertical depth of the slip surface (m), γ_w is the weight of water (kN/m^3), α is the angle of slope ($^\circ$), c' is effective cohesion (kPa).

4. Results

4.1. Spatial deformation patterns of ALDS

Using advanced SBAS method helps to better illuminate the

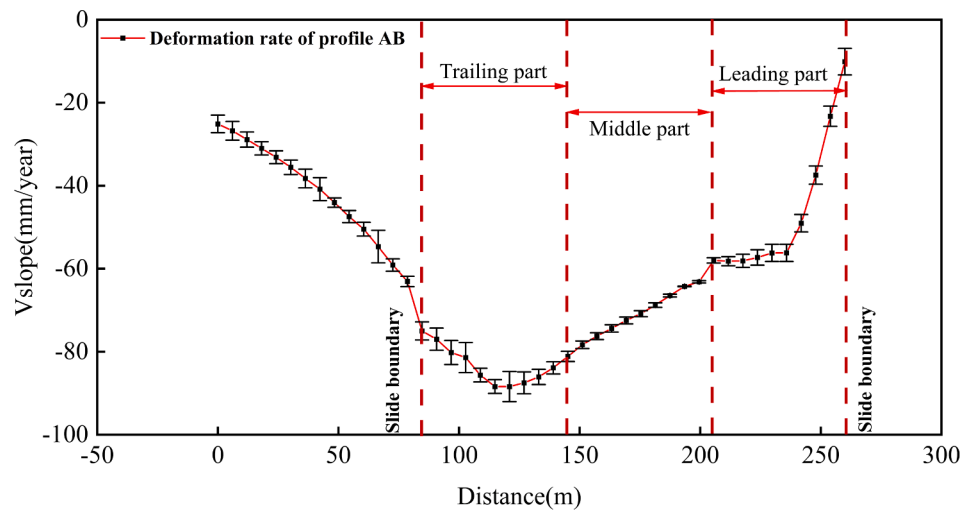


Fig. 6. Annual average deformation rate along the downslope direction of profile AB marked in Fig. 1. The red dashed line divides the deformation rate into three parts: the trailing part, the middle part, and the leading part. The error bars depict the annual deformation rate standard deviations.

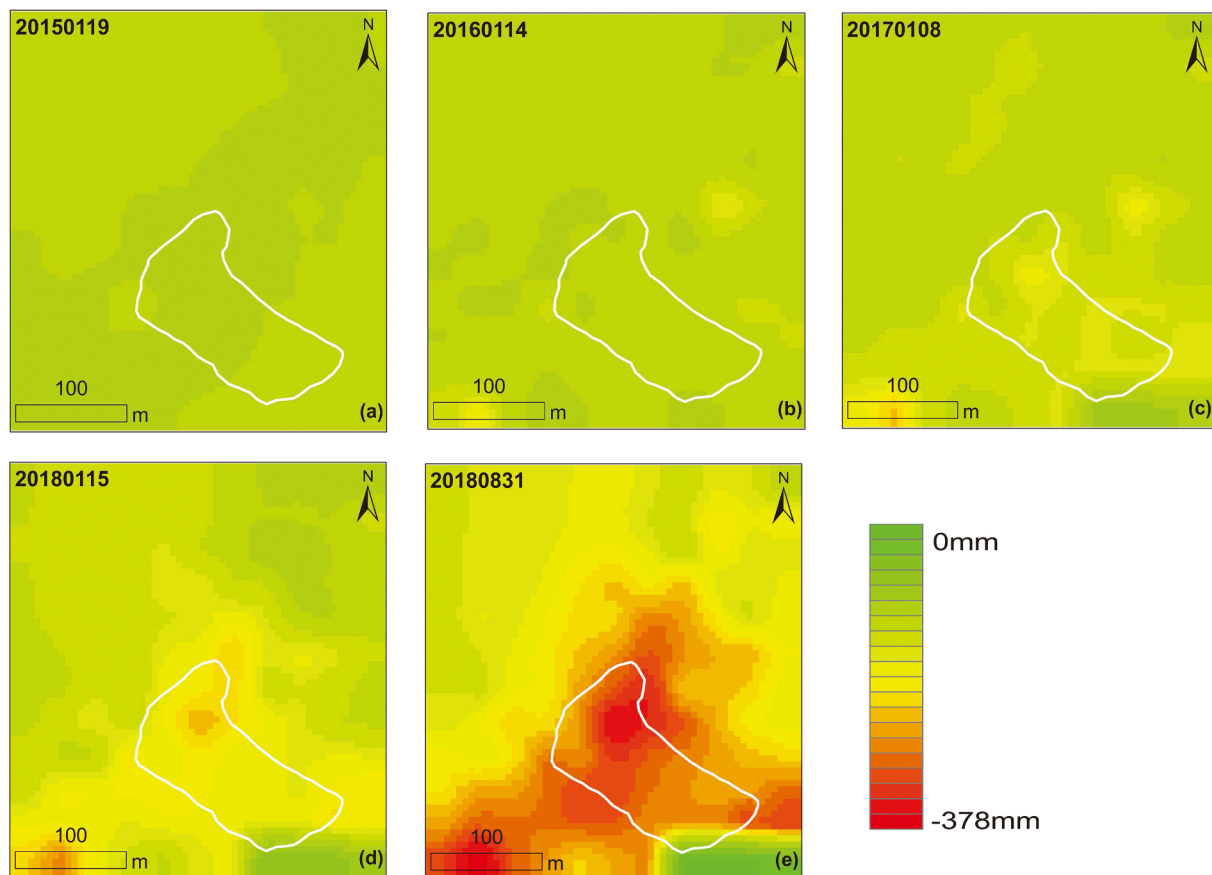


Fig. 7. Development of accumulative downslope deformation on the ALDS from January 19, 2015, to August 31, 2018. The white line represents the sliding boundary. The SAR image of reference is captured on October 27, 2014.

deformation patterns of the ALDS. To uncover the spatial-temporal characteristics of the ALDS, we have generated a deformation rate map of ALDS in the downslope direction, as illustrated in Fig. 5. Our analyses show that deformation rate in the trailing part is the largest, whereas the leading part's area of the ALDS is relatively small (Fig. 5). The above deformation feature differs from traditional pull-type landslides (Zhou et al., 2020). In addition, we detect distinct deformation signals near the landslide boundary, but these regions are not slides, which are created

by frozen soil thawing and settlement. InSAR could simultaneously acquire these two signals.

To further study spatial deformation patterns of the ALDS, we extract the deformation rate by the downslope deformation map along profile A-B, as shown by the dotted lines in Fig. 5. Fig. 5 shows that profile A-B is approximately 260 m long, stretching from the head scarp to the toe of the ALDS. The ALDS can be separated into three parts in space based on the change in velocity of the A-B profile: the trailing part has the

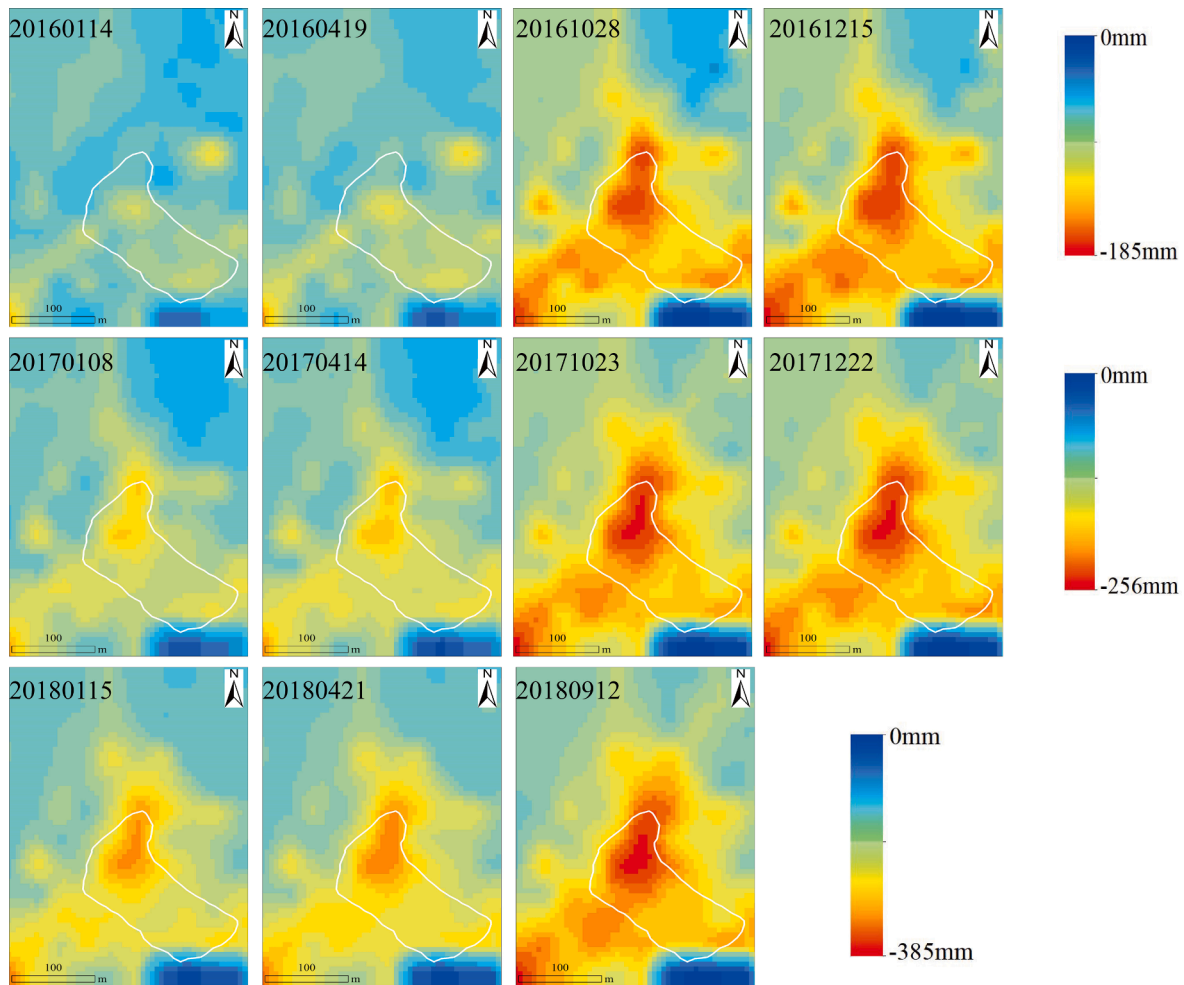


Fig. 8. Time series deformation maps of accumulative downslope deformation on the ALDS from January 14, 2016 to September 12, 2018. The white line represents the sliding boundary. The SAR image of reference was captured on January 19, 2015.

maximum sliding velocity, the middle part follows in the second, and the leading part has the lowest sliding velocity (Fig. 6). The trailing, middle, and leading parts have a typical deformation rate of -83 , -69 , and -46 mm/year, respectively. In addition, the upslope section's deformation rate is relatively slower than that of the internal ALDS (Fig. 6).

4.2. Temporal deformation patterns of the ALDS

The temporal deformation pattern of ALDS shows significant inter-annual difference (Fig. 7). The deformation rate of the ALDS is slow from January 2015 to January 2016, but accelerates from January 2016 to January 2018, and intensifies substantially after January 2018. Tension fractures form after the sliding body moves, and the development of tension cracks will promote water infiltration which grows as precipitation increases. The variations in water infiltration led to changes in both the shear strength and pore water pressure near the sliding surface (pore water pressure rises and shear strength falls as infiltration increases), which will eventually result in interannual differences in the deformation patterns (Fig. 7).

There are pronounced seasonal deformation characteristics in the ALDS compared with landslides occurring in the non-permafrost region (Fig. 8). The ALDS is most active during the thawing season, with no noticeable deformations during the freezing season (Fig. 8). The above deformation characteristic represents a departure from ordinary landslides. Soil freeze-thaw cycle and periodic atmospheric (precipitation and air temperature) alternation (Fig. 9) are the primary reasons for seasonal deformation. During the thawing period, soil moisture

increases due to high-temperature (Fig. 9a) melting and concentrated precipitation (Fig. 9b), leading to a decrease in shear strength and increase in deformation rate. Conversely, the soil freezes gradually under the action of negative temperature (Fig. 9a). The decrease in slope deformation rate is associated with an increase in soil shear strength in the freezing period.

4.3. Dynamics of ALDS

To investigate the dynamics of the ALDS, we select three points (which are located at the middle of each section) (labeled in Fig. 1) of the ALDS to generate time series (Fig. 10) showing that the landslide consists of three distinct stages: moderate creep stage, steady creep stage, and rapid collapse stage.

Moderate creep stage: During the disturbance of external conditions such as climate change and slope toe digging, the active layer slowly creeps under the influence of gravity from January 2015 to May 2016 at an average deformation rate of 2.6 mm/month. High-resolution optical remote sensing images cannot identify this stage due to the tiny tension cracks, but InSAR technology can detect this slow creep (Fig. 10).

Steady creep stage: In this stage, average deformation rate is 10.1 mm/month and the slope is equalized under the impact of friction in this stage. This stage lasted from May 2016 till April 2018. As tensile cracks develop, precipitation infiltration, and heat conduction rise, as does the thawing and deformation rate of the slope. Since this stage occurs before slope failure, it is a crucial monitoring phase for early warning of landslides and has great significance for warning of ALDS.

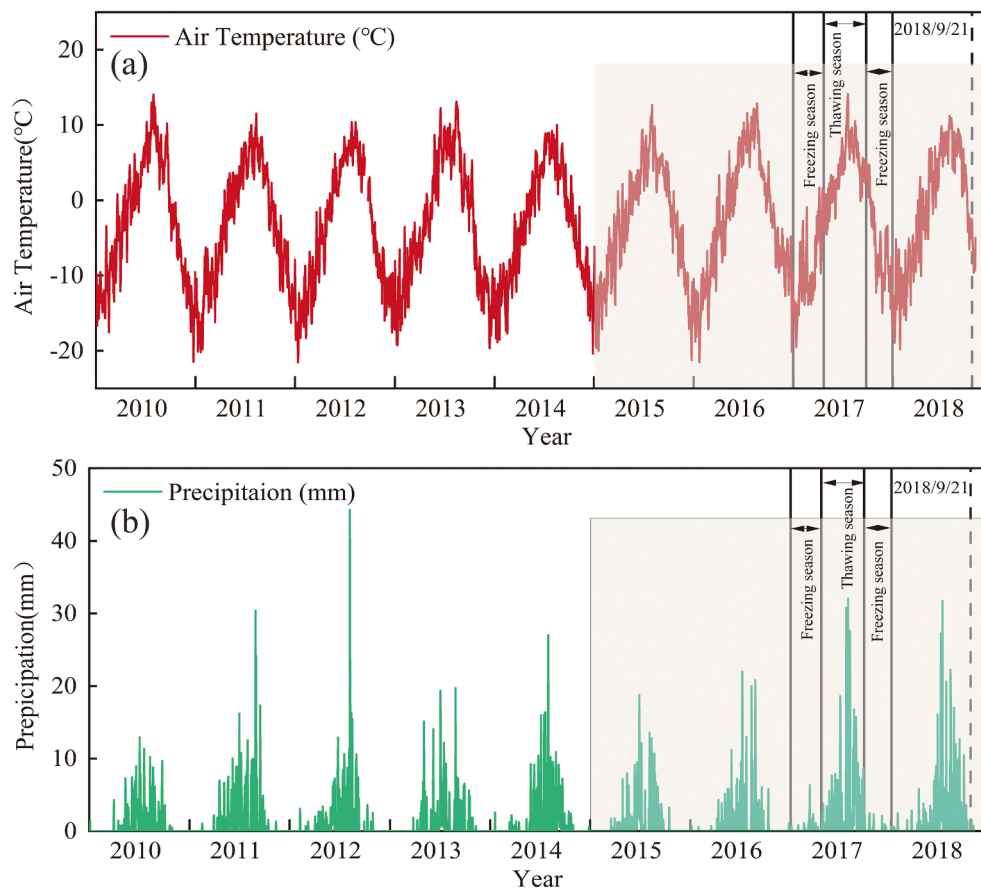


Fig. 9. Meteorological information during 2010–2018. (a) Daily air temperature variations during 2010–2018. (b) Daily precipitation variation. The black dashed lines represent the time when the ALDS occurred. The gray bars represent the timespan of the study.

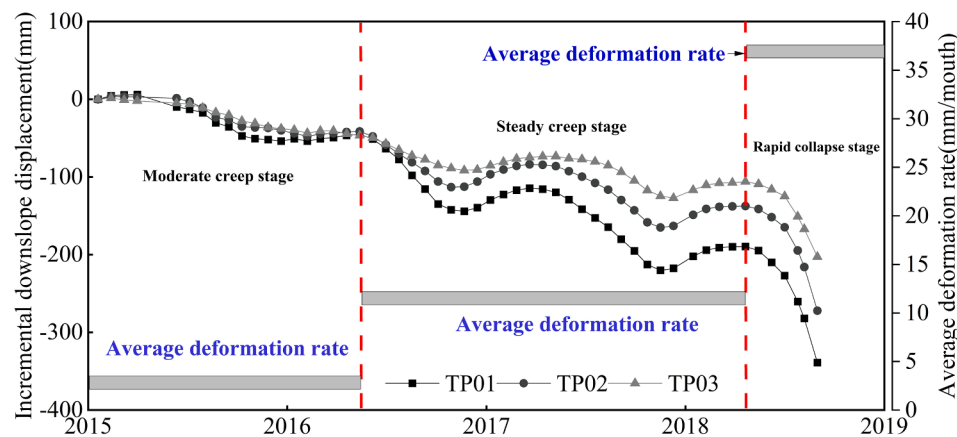


Fig. 10. Incremental displacement of three time series points labeled in Fig. 1. The red dashed line divides the accumulative displacement curve into three stages: moderate creep stage, steady creep stage, and rapid collapse stage.

Rapid collapse stage: This stage lasted from April to August 31, 2018, with an average deformation rate of 33.5 mm/month. The deformation rate in this stage increases dramatically. When the shear strength reaches the critical value, the failure of slope occurs. Moreover, we can also use this dramatic acceleration stage as an important indicator for ALDS warning.

5. Discussion

5.1. Causal analysis of ALDS

In general, extreme precipitation events (McConchie, 2004; Hawke and Mcconchie, 2011) are the primary cause of the landslide, whereas, in permafrost areas, Temperature also plays an essential role in the formation of landslides. Based on meteorological and borehole data, the positive accumulated air temperature and ground surface temperature make 2018 the second warmest thaw season in the four-year period,

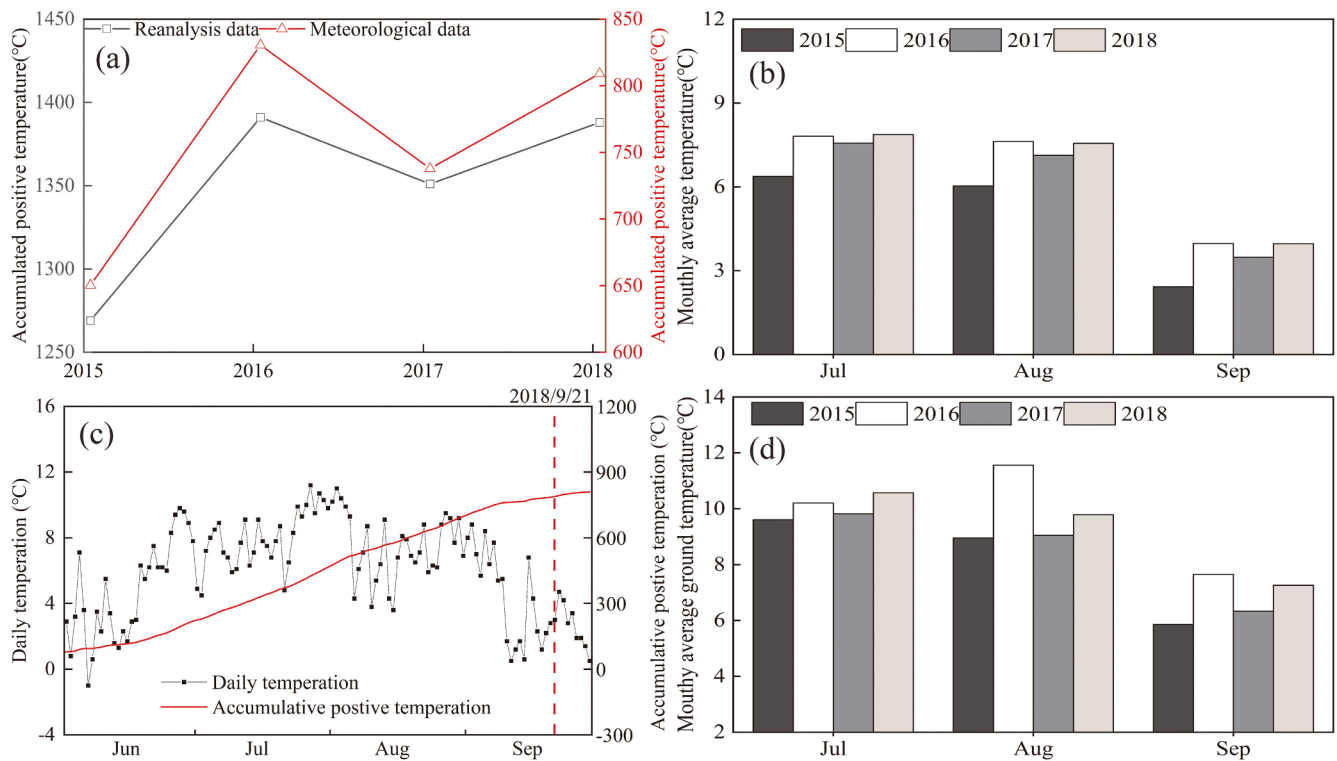


Fig. 11. (a) Accumulated positive temperature at Beiluhe weather station and National Tibetan Plateau Data Center (2015–2018). (b) The monthly average temperature at Beiluhe weather station. (c) Daily temperature and accumulative temperature at Beiluhe weather station from June to September 2018. The ALDS occurred at the time indicated by the red dashed line. (d) The monthly average temperature at National Tibetan Plateau Data Center.

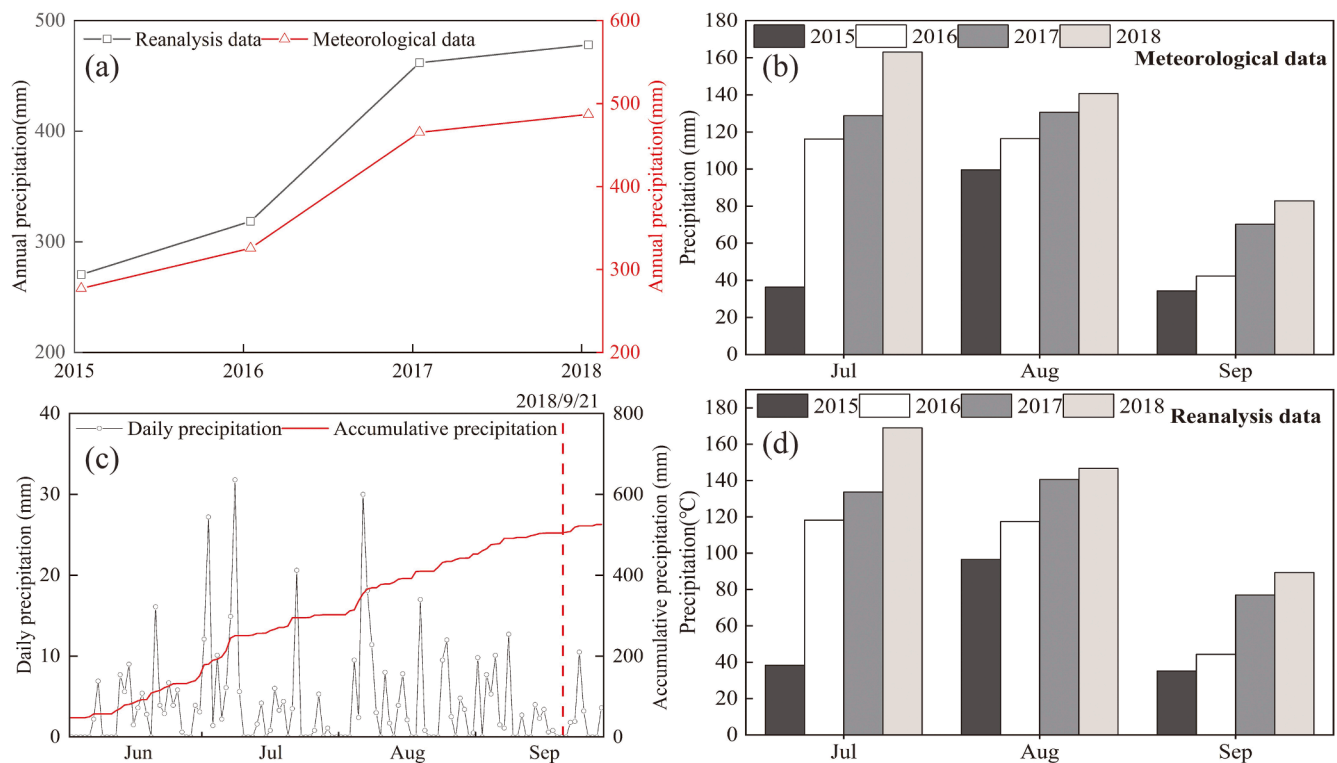


Fig. 12. (a) Annual accumulation precipitation at Beiluhe weather station and National Tibetan Plateau Data Center (2015–2018). (b) Monthly precipitation at Beiluhe weather station. (c) Daily and accumulative precipitation at Beiluhe weather station from June to September 2018. The ALDS occurred at the time indicated by the red dashed line. (d) Monthly precipitation at National Tibetan Plateau Data Center.

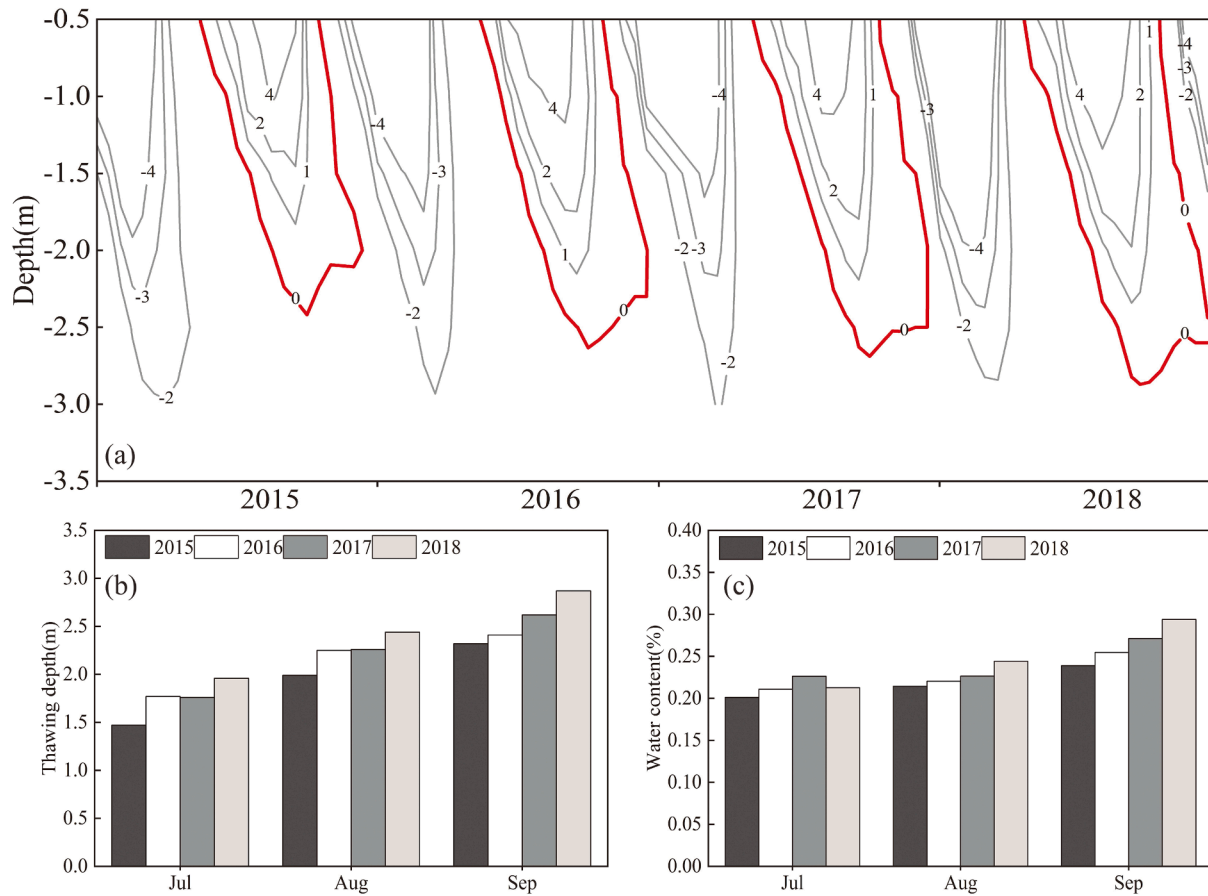


Fig. 13. (a) Isotherm acquired by borehole soil ground temperature at different depths. The red line represents 0 °C isotherm. (b) Thawing depth acquired by 0 °C isotherm. (c) The monthly soil water content (volumetric content) at Beiluhe weather station.

nearly identical to 2016 (Fig. 11). The annual accumulative precipitation from 2015 to 2018 increased with the maximum cumulative precipitation of 478 mm measured in 2018, followed by 461 mm in 2017. In addition, the average monthly precipitation from July to September 2018 is higher than in other years (Fig. 12bd). Therefore, 2018 is marked by both heavy precipitation and warm temperatures in the 4-year period, which lead to ALDS in the region (Jiang et al., 2022). Large-scale precipitation and high air temperatures are mainly focused on the two-month preceding the slope failure (Fig. 11c, Fig. 12c), indicating that precipitation and high temperatures did not directly cause the landslide. In addition, the thawing depth and soil water content (volumetric content) at 2.4 m from July to September 2018 are greater than those in other years (Fig. 13bc).

Although high air temperature and precipitation do not directly cause the landslide, they alter the convective heat transfer in the active layer (Jiang et al., 2022), further leading to an increase in thawing depth and soil moisture content at the base of the active layer. Meanwhile, a significant amount of underground ice forms at the base of the active layer during the freezing season due to elevated levels of precipitation in 2017 (Lewkowicz and Harris, 2005a, 2005b), which thaw in the warmer months of 2018. Furthermore, the alteration of the 0 °C isotherm (as depicted in Fig. 13a) illustrates that once the maximum thawing depth is reached, freezing commences both from the bottom of the active layer upwards and from the top downwards. This two-way freezing process, which can, on the one hand, encourage underground ice form and, on the other hand, alter the water from weight water to confined water when the ground surface freezes downwards, producing excessive pore water pressure, also contributes to slope instability in permafrost environments (Yang et al., 2017; Hao et al., 2023).

5.2. Correlation of triggers and ALDS movement

To explore the relationship between ALDS movement and triggers, we compare air temperature, precipitation, and thawing process with the deformation acquired by InSAR for the observation point TP01 (Fig. 1). We use daily air temperature and precipitation measurements to calculate the values during the same periods as the InSAR observations. After that, we compare extracted values with the cumulative displacement and deformation rate for each epoch obtained from InSAR (Fig. 14).

We find significant correlations between the thawing process, precipitation, accumulative air temperature, and deformation rate. During the thawing season, the deformation rate increases in corresponding the rise of air temperature (Fig. 14b), precipitation (Fig. 14a) and thawing depth (Fig. 14c), ultimately diminishing the shear strength at the sliding surface and raising the sliding force (weight of the landslide bodies) (Iverson, 2000; Jiang et al., 2022), result in the increase of deformation rate (Fig. 14). However, in the freezing season, the soil gradually freezes under the action of negative air temperature (Fig. 14b). The decrease of deformation rate reflects in a corresponding rise in shear strength rises due to soil freezing process (Jiang et al., 2022). We also find the deformation rate of the ALDS is extremely congruent with precipitation and temperature with a delay of approximately one month due to the lag of heat transfer and precipitation infiltration, while the thawing depth is compatible with the change in deformation rate. Quantitatively, we put forward the relationship among precipitation, air temperature and deformation rate to investigate the causal relationship further. There are 0.32 and 0.43 correlations between deformation rate and precipitation and temperature (Fig. 15a, Fig. 15b), and the correlation of deformation rate and thawing depth is 0.58 (Fig. 15c), which indicates thawing depth

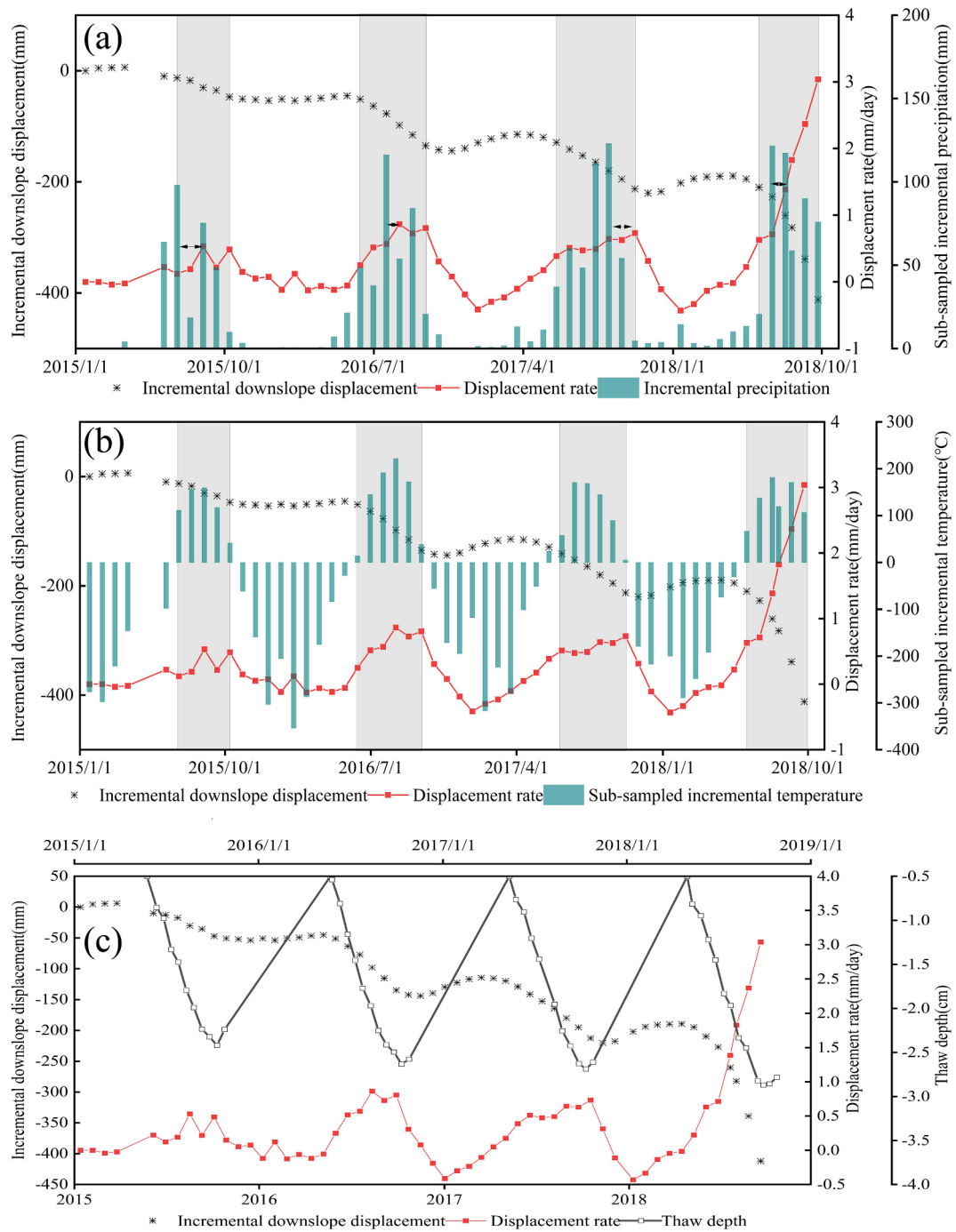


Fig. 14. The correlation among sub-sampled incremental precipitation, sub-sampled incremental precipitation, thawing depth, and deformation rate acquired by InSAR for the observation site TP01 (labeled in Fig. 1). The time period of the sliding acceleration is represented by the gray bars, and the gaps from the peak of precipitation to the point of sliding acceleration is represented by the blue arrows.

change is more likely to be the primary trigger of ALDS movement in our study case. Moreover, we discover two evident acceleration periods in which the first instance of accelerated moving on the ALDS in 2016 links with elevated air temperatures during the thawing season (Fig. 11a). The second acceleration episode correlates with high temperature and precipitation (Fig. 11a, Fig. 12a) in the thawing season of 2018.

5.3. Analysis of landslide mechanism

5.3.1. Migration process and classification

Based on the temporal deformation map of the ALDS obtained by

InSAR (Fig. 7), we capture the development process of the ALDS. The deformation first occurs at the leading part of the slope, while neither the trailing nor middle part of the slope exhibit significant sliding (Fig. 7a) at this stage. This deformation difference will generate tensile cracks at the junction, accelerating precipitation infiltration, heat transfer and underground ice melting in the trailing and middle part, further promoting the trailing and middle interests of the slope to start sliding (Fig. 7b). The upper portion of the landslide trailing edge is relatively stable at this stage. The deformation difference leads to tensile cracks at the junction of the landslide trailing edge, which accelerates the sliding of the trailing part of the slope (Fig. 7c, Fig. 7d). Additionally,

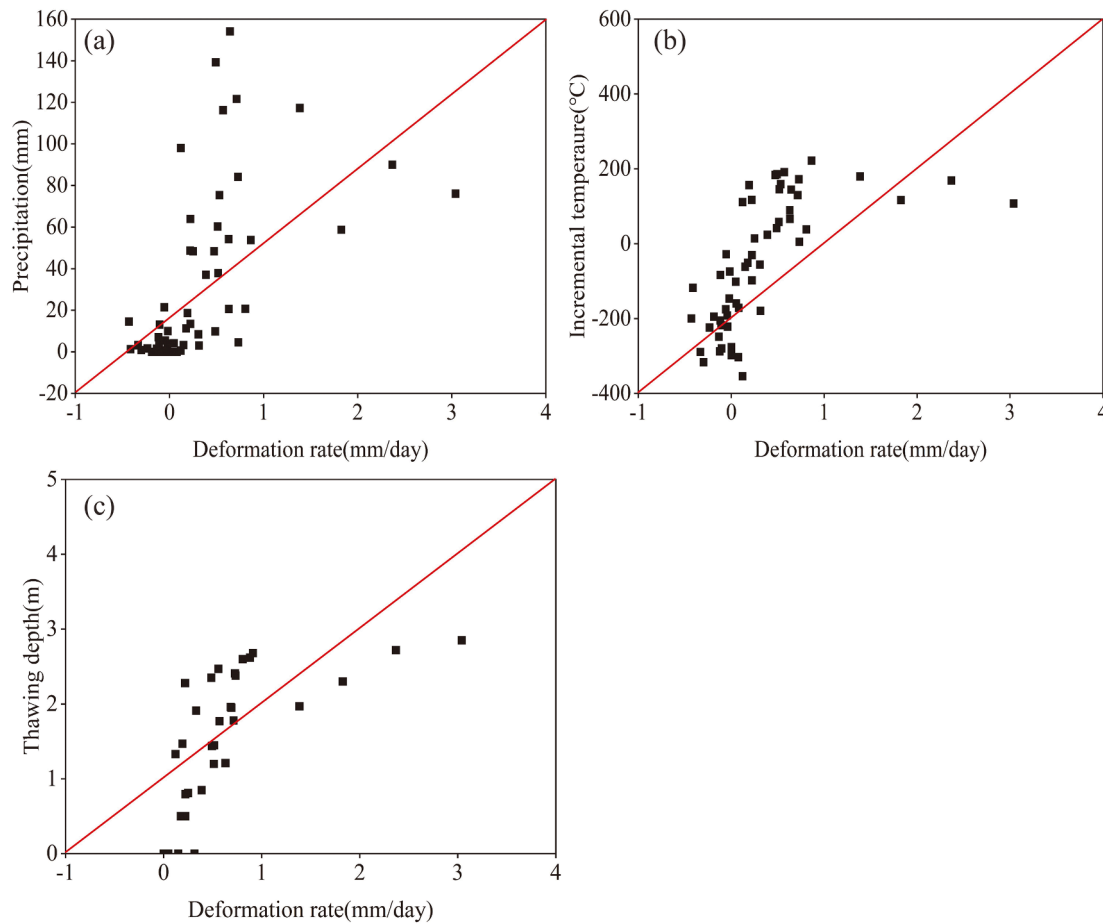


Fig. 15. The correlations between deformation rate and (a) precipitation, (b) incremental temperature, (c) thawing depth for each InSAR epoch ($P < 0.05$).

Table 3

Deformation rate (mm/month) and Safety factor for September from 2015 to 2018.

Year	2015	2016	2017	2018
Deformation rate	-15.2	-24.2	-23.6	-60.3
Safety factor	1.1356	1.0977	1.0961	1.0273

the development of fractures will be accelerated by the increase in deformation differences between the trailing and middle part of the ALDS and the upper area of the trailing edge, significantly accelerating the deformation of the trailing and middle parts of the sliding mass (Fig. 7e). The ALDS is not a traditional pull-type or push-type landslide based on the analyses of migration process. In the slow creep stage, it manifests itself as a pull-type landslide (Fig. 7a); in the accelerated creep and ring-breaking stages, it manifests as a push-type landslide (Fig. 7c, Fig. 7d, Fig. 7e). It is a mixed-type landslide caused by deformation differences in the different migration process.

5.3.2. Analysis of slope stability

Water table in the active layer is dependent on precipitation. We presume that September's water table remains constant due to the relatively low precipitation in September from 2015 to 2018 (Fig. 12b, Fig. 12d). Using Eq. (6), we calculate the safety factor corresponding to the maximal depth of melting in September from 2015 to 2018. Table 3 displays the safety factor and deformation rate (TP01). The table shows that in September 2018, the deformation rate dramatically accelerated, with an increase of 154 %, while the safety factor decreased slightly in September 2018, with a decrease of 6.2 %. This indicates that the

cumulative effect of deformation and creep damage may be the leading reason for slope instability in the study region. Cumulative deformation will encourage the formation of fissures, accelerate the melting of underground ice, further raise the penetration of precipitation, and weaken the shear strength of sliding surfaces (Tong and David, 2016). Moreover, once the displacement of frozen soil surpasses a specific threshold and exceeds the limit of strain damage, the frozen soil transitions into a stage characterized by accelerated creep, leading to internal structural deterioration. Once the damage level surpasses a certain threshold, the frozen soil movement rate increases abruptly, which leads to the failure of the slope (Shi et al., 2020; Li et al., 2018).

6. Conclusion

This study utilizes SBAS to determine the creep characteristics of ALDS in the Fenghuoshan Mountains. From 2014 to 2018. The thermal-spatial deformation and motion patterns are examined using the Sentinel-1A data. In addition, the mechanism of ALDS and the relationship between the rate of deformation and triggers are investigated. We conclude that:

- (1) The deformation rate of ALDS presents a distinct seasonal variation pattern in the thermal dimension; the deformation varies substantially among different parts of ALDS.
- (2) Movement of ALDS in regions of permafrost can be separated into three stages: moderate creep stage, steady creep stage, and rapid collapse stage based on the deformation rate. The accurate identification of the steady creep stage is essential for early warning of the ALDS.

- (3) Heavy summer precipitation in 2017 and 2018 contributed to the development of underground ice while high air temperature causes the thaw plane to reach the ice-rich zone, and confined water induced by the two-way freezing process resulted in ALDS.
- (4) Thawing depth is generally consistent with the variation in deformation rate, and the relationship between deformation rate and precipitation and air temperature has a one-month time lapse, indicating that thawing depth variations is the direct trigger of ALDS.
- (5) The ALDS is a mixed-type landslide (combined with pull-type and push-type landslides) caused by deformation differences in various migration parts, with the cumulative effect of deformation and creep damage playing important roles in triggering ALDS.

In summary, this study provides a methodical procedure that employs the InSAR technique for deformation monitoring, creep model analysis, trigger factor confirmation, and mechanism examination of ALDS occurred in the permafrost regions. This procedure is well relevant for the creation a system of early warning for landslides that occur in permafrost regions under extreme weather conditions.

CRediT authorship contribution statement

Fei Wang: Conceptualization, Methodology, Writing – original draft, Funding acquisition. **Zhi Wen:** Conceptualization, Funding acquisition, Project administration, Supervision. **Qiang Gao:** Investigation, Validation. **Qihao Yu:** Data curation, Funding acquisition. **Desheng Li:** Resources, Software, Writing – review & editing. **Liangzhi Chen:** Data curation, Writing – review & editing.

Declaration of competing interest

The authors declare that they have no known competing financial interests or personal relationships that could have appeared to influence the work reported in this paper.

Data availability

Data will be made available on request.

Acknowledgments

This research project was supported by the Natural Science Foundation of China (Grant No. 42272332, 42371140, 42301163, and 41971087), Major Science and technology project of Gansu Province (Grant No. 23ZDWA005) and Excellent Doctoral Programme of Gansu Province (Grant No. 23JRRA602). The meteorological data were obtained from the Beiluhe Observation and Research Station on Frozen Soil Engineering and Environment in Qinghai-Tibet Plateau (<http://www.beiluhe.ac.cn/>) and the reanalyzed data was freely downloaded from the National Tibetan Plateau Data Center (<https://data.tpdc.ac.cn/>).

References

- Ambrosi, C., Strozzi, T., Scapozza, C., Wegmüller, U., 2018. Landslide hazard assessment in the Himalayas (Nepal and Bhutan) based on Earth-Observation data. *Eng. Geol.* 237, 217–228. <https://doi.org/10.1016/j.enggeo.2018.02.020>.
- Baran, I., Stewart, M.P., Kampes, B.M., Perski, Z., Lilly, P., 2003. A modification to the Goldstein radar interferogram filter. *IEEE Trans. Geosci. Remote Sens.* 41, 1–5. <https://doi.org/10.1109/TGRS.2003.817212>.
- Berardino, P., Fornaro, G., Lanari, R., Sansosti, E., 2002. A new algorithm for surface deformation monitoring based on small baseline differential SAR interferograms. *IEEE Trans. Geosci. Remote Sens.* 40, 2375–2383. <https://doi.org/10.1109/TGRS.2002.803792>.
- Calvello, M., Peduto, D., Arena, L., 2017. Combined use of statistical and InSAR data analyses to define the state of activity of slow-moving landslides. *Landslides* 14, 473–489. <https://doi.org/10.1007/s10346-016-0722-6>.
- Chadburn, S.E., Burke, E.J., Cox, P.M., Friedlingstein, P., Hugelius, G., Westermann, S., 2017. An observation-based constraint on permafrost loss as a function of global warming. *Nat. Clim. Chang.* 7, 340–344. <https://doi.org/10.1038/nclimate3262>.
- Chen, F., Hui, L., Zhen, L., Quan, C., Zhou, J., 2012. Interaction between permafrost and infrastructure along the Qinghai-Tibet railway detected via jointly analysis of C- and L-band small baseline SAR interferometry. *Remote Sens. Environ.* 123, 532–540. <https://doi.org/10.1016/j.rse.2012.04.020>.
- Chen, J., 2018. The active layer moisture monitoring dataset of Qinghai-Tibet Plateau Beiluhe meteorological station (2017.1–2018.10). National Tibetan Plateau/Third Pole Environment Data Center. <https://doi.org/10.11888/Geocry.tpdc.270461>.
- Cigna, F., Bateson, L.B., Jordan, C.J., Dashwood, C., 2014. Simulating SAR geometric distortions and predicting persistent scatterer densities for ERS-1/2 and ENVISAT C-band SAR and InSAR applications: Nationwide feasibility assessment to monitor the landmass of Great Britain with SAR imagery. *Remote Sens. Environ.* 152, 441–466. <https://doi.org/10.1016/j.rse.2014.06.025>.
- Costard, F., Dupeyrat, L., Séjourné, A., Bouchard, F., Fedorov, A., Saint-Bézar, B., 2021. Retrogressive thaw slumps on ice-rich permafrost under degradation: Results from a large-scale laboratory simulation. *Geophys. Res. Lett.* 48, 146–159. <https://doi.org/10.1029/2020GL091070>.
- Fattah, H., Amelung, F., 2015. InSAR bias and uncertainty due to the systematic and stochastic tropospheric delay. *Journal of Geophysical Research: Solid Earth: JCR120*. 12, 8758–8773. <https://doi.org/10.1002/2015JB012419>.
- Ferretti, A., Prati, C., Rocca, F., 2001. Permanent scatterers in SAR interferometry. *IEEE Trans. Geosci. Remote Sens.* 39, 1528–1530. <https://doi.org/10.1109/IGARSS.1999.772008>.
- Ferretti, A., Fumagalli, A., Novati, F., Prati, C., Rocca, F., Rucci, A., 2011. A new algorithm for processing interferometric data-stacks: SqueeSAR. *IEEE Trans. Geosci. Remote Sens.* 49, 3460–3470. <https://doi.org/10.1109/TGRS.2011.2124465>.
- Goldstein, R.M., Werner, C.L., 1998. Radar interferogram filtering for geophysical applications. *Geophys. Res. Lett.* 25, 4035–4038. <https://doi.org/10.1029/1998GL900033>.
- Gong, W., Darrow, M.M., Meyer, F.J., Daanen, R.P., 2019. Reconstructing movement history of frozen debris lobes in northern Alaska using satellite radar interferometry. *Remote Sens. Environ.* 221, 722–740. <https://doi.org/10.1016/j.rse.2018.12.014>.
- Gray, A.L., Mattar, K.E., Sofko, G., 2000. Influence of ionospheric electron density fluctuations on satellite radar interferometry. *Geophys. Res. Lett.* 27, 1451–1454. <https://doi.org/10.1029/2000GL000016>.
- Guo, B., Liu, Y.F., Fan, J.F., Lu, M., Zang, W.Q., Liu, C., Wang, B.Y., Huang, X.Z., Lai, J.B., Wu, H.W., 2023. The salinization process and its response to the combined processes of climate change–human activity in the Yellow River Delta between 1984 and 2022. *Catena* 231, 1–13. <https://doi.org/10.1016/j.catena.2023.107301>.
- Guo, L., You, Y.H., Yu, Q.H., Shi, Z.Y., Li, H.B., Wang, X.B., 2021. Field investigation on the influence of periglacial processes on pile foundations on the Qinghai-Tibet Plateau. *Permafrost. Periglac. Process.* 32, 335–348. <https://doi.org/10.1002/ppp.2092>.
- Hao, X.Y., Ma, W., Feng, W.J., Wen, Z., Zhang, L.H., Chen, S.J., 2023. Investigation on the frost heave-induced pressure and hydro-thermal processes in freezing soil under rigid constraint and hydraulic pressure. *Eng. Geol.* 323, 107238. <https://doi.org/10.1016/j.enggeo.2023.107238>.
- Hao, J.M., Wu, T.H., Wu, X., Hu, G., Ma, W., 2019. Investigation of a small landslide in the Qinghai-Tibet plateau by InSAR and absolute deformation model. *Remote Sens.* 11, 2126. <https://doi.org/10.3390/rs11182126>.
- Hawke, R., McConchie, J., 2011. In situ measurement of soil moisture and pore-water pressures in an ‘incipient’ landslide: Lake Tutira, New Zealand. *J. Environ. Manage.* 92, 266–274. <https://doi.org/10.1016/j.jenvman.2009.05.035>.
- Hooper, A., Zebker, H., Segall, P., Kampes, B., 2004. A new method for measuring deformation on volcanoes and other natural terrains using InSAR persistent scatterers. *Geophys. Res. Lett.* 31. <https://doi.org/10.1029/2004GL021737>.
- Iverson, R.M., 2000. Landslide triggering by rain infiltration. *Water Resour. Res.* 36, 1897–1910. <https://doi.org/10.1029/2000WR900090>.
- Jiang, G.L., Gao, S., Lewkowicz, A.G., Zhao, H.T., Pang, S.J., Wu, Q.B., 2022. Development of a rapid active layer detachment slide in the Fenghuoshan Mountains, Qinghai-Tibet Plateau. *Permafrost Periglacial Process* 1–12. <https://doi.org/10.1002/ppp.2151>.
- Jorgenson, M.T., Osterkamp, T.E., 2005. Response of boreal ecosystems to varying modes of permafrost degradation. *Can. J. For. Res.* 35, 2100–2111. <https://doi.org/10.1139/x05-153>.
- Kokelj, S.V., Lacelle, D., Lantz, T.C., Tunnicliffe, J., Malone, L., Clark, I.D., Chin, K.S., 2013. Thawing of massive ground ice in mega slumps drives increases in stream sediment and solute flux across a range of watershed scales. *Geophys. Res. Atmos.* 118, 1–12. <https://doi.org/10.1002/jgrf.20063>.
- Lewkowicz, A.G., 2010. Dynamics of active-layer detachment failures, Fosheim Peninsula, Ellesmere Island, Nunavut, Canada. *Permafrost & Periglacial Processes* 2010 (18), 89–103. <https://doi.org/10.1002/ppp.578>.
- Lewkowicz, A.G., Harris, C., 2005a. Frequency and magnitude of active-layer detachment failures in discontinuous and continuous permafrost, northern Canada. *Permafrost. Periglac. Process.* 16, 115–130. <https://doi.org/10.1002/ppp.522>.
- Lewkowicz, A.G., Harris, C., 2005b. Morphology and geotechnique of active-layer detachment failures in discontinuous and continuous permafrost, northern Canada. *Geomorphology* 69, 275–297. <https://doi.org/10.1016/j.geomorph.2005.01.011>.
- Lewkowicz, A.G., Way, R.G., 2019. Extremes of summer climate trigger thousands of thermokarst landslides in a High Arctic environment. *Nat. Commun.* 10, 1329. <https://doi.org/10.1038/s41467-019-09314-7>.
- Li, D., Chen, J., Zhou, Y., 2018. A Study of Coupled Creep Damaged Constitutive Model of Artificial Frozen Soil. *Adv. Mater. Sci. Eng.* 1–9. <https://doi.org/10.1155/2018/7458696>.

- Li, D.S., Wen, Z., Luo, J., Zhang, M., Chen, B., 2019. Slope failure induced by cold snap and continuous precipitation in the seasonal frozen area of Qinghai-Tibet Plateau. *The Science of the Total Environment*. 694, 133547.1-133547.10. <https://doi.org/10.1016/j.scitotenv.2019.07.353>.
- Li, M., Zhang, L., Ding, C., Li, W., Luo, H., Liao, M., Xu, Q., 2020. Retrieval of historical surface displacements of the Baige landslide from time-series SAR observations for retrospective analysis of the collapse event. *Remote Sens. Environ.* 2020 (240), 336–349. <https://doi.org/10.1016/j.rse.2020.111695>.
- Liljedahl, A.K., Boike, J., Daanen, R.P., Fedorov, A.N., Frost, G.V., Grosse, G., Necsoiu, M., 2016. Pan-Arctic ice-wedge degradation in warming permafrost and its influence on tundra hydrology. *Nat. Geosci.* 9, 312–318. <https://doi.org/10.1038/ngeo2674>.
- Luo, J., Niu, F.J., Lin, Z., Liu, M., Yin, G., 2019. Recent acceleration of thaw slumping in permafrost terrain of Qinghai-Tibet Plateau: An example from the Beiluhe Region. *Geomorphology* 341, 79–85. <https://doi.org/10.1016/j.geomorph.2019.05.020>.
- Ma, W., Niu, F.J., Satoshi, A., Jin, D.W., 2006. Slope instability phenomena in permafrost regions of Qinghai-Tibet Plateau, China. *Landslides* 3, 260–264. <https://doi.org/10.1007/s10346-006-0045-0>.
- Massonnet, D., Feigl, K.L., 1998. Radar interferometry and its application to changes in the Earth's surface. *Rev. Geophys.* 36, 441–500. <https://doi.org/10.1029/97RG03139>.
- McConchie, J.A., 2004. The influence of earthflow morphology on moisture conditions and slope instability. *Hydrol.* 43, 3–17. <http://www.jstor.org/stable/43944911>.
- McRoberts, E.C., Morgenstern, N.R., 1974. Stability of slopes in frozen soil. *Int. J. Rock Mech. Min. Sci. Geomechanics*. 11, 554–573. <https://doi.org/10.1139/t74-058>.
- Nelson, F.E., Anisimov, O.A., Shiklomanov, N.I., 2001. Subsidence risk from thawing permafrost-The threat to man-made structures across regions in the far north can be monitored. *Nature* 410, 889–890. <https://doi.org/10.1038/35073746>.
- Niu, F.J., Luo, J., Lin, Z., Ma, W., Lu, J., 2012. Development and thermal regime of a thaw slump in the Qinghai-Tibet plateau. *Cold Reg. Sci. Technol.* 83, 131–138. <https://doi.org/10.1016/j.coldregions.2012.07.007>.
- Niu, F.J., Luo, J., Lin, Z., Fang, J., Liu, M., 2016. Thaw-induced slope failures and stability analyses in permafrost regions of the Qinghai-Tibet Plateau, China. *Landslide* 13, 55–65. <https://doi.org/10.1007/s10346-014-0545-2>.
- Notti, D., Herrera, G., Bianchini, S., 2014. A methodology for improving landslide PSI data analysis. *Int. J. Remote Sens.* 35, 2186–2214. <https://doi.org/10.1080/01431161.2014.889864>.
- Novellino, A., Cigna, F., Sowter, A., Ramondini, M., Calcaterra, D., 2017. Exploitation of the intermittent SBAS (ISBAS) algorithm with COSMO-SkyMed data for landslide inventory mapping in north-western Sicily, Italy. *Geomorphology* 280, 153–166. <https://doi.org/10.1016/j.geomorph.2016.12.009>.
- Peng, X., Zhang, T., Frauenfeld, O.W., Wang, K., Luo, D.L., Cao, B., Wu, Q.B., 2018. Spatiotemporal changes in active layer thickness under contemporary and projected climate in the Northern Hemisphere. *J. Clim.* 31, 251–266. <https://doi.org/10.1175/JCLI-D-16-0721.1>.
- Peng, S., 2019. 1-km monthly mean temperature dataset for China (1901–2021). National Tibetan Plateau/Third Pole Environment Data Center. <https://doi.org/10.11888/Meteoro.tpd.270961>.
- Pepe, A., Lanari, R., 2006. On the extension of the minimum cost flow algorithm for phase unwrapping of multitemporal differential SAR interferograms. *Geosci. Remote Sens., IEEE Trans.* 44, 2374–2383. <https://doi.org/10.1109/TGRS.2006.873207>.
- Ran, Y., Li, X., Cheng, G., 2018. Climate warming over the past half century has led to thermal degradation of permafrost on the Qinghai-Tibet Plateau. *Cryosphere* 12, 595–608. <https://doi.org/10.5194/tc-12-595-2018>.
- Reyes-Carmona, C., Barra, A., Galve, J.P., Monserrat, O., Pérez-Peña, J.V., Mateos, R.M., Notti, D., Ruano, P., Millares, A., López-Vinielles, J., 2020. Sentinel-1 DInSAR for Monitoring Active Landslides in Critical Infrastructures: The Case of the Rules Reservoir (Southern Spain). *Remote Sen.* 12, 809. <https://doi.org/10.3390/rs12050809>.
- Schaefer, K., Zhang, T., Bruhwiler, L., Barrett, A.P., 2011. Amount and timing of permafrost carbon release in response to climate warming. *Tellus b: Chem. Phys.* Meteorol. 63, 165–180. <https://doi.org/10.1111/j.1600-0889.2011.00527.x>.
- Schlögl, R., Doubre, C., Malet, J.P., Masson, F., 2015. Landslide deformation monitoring with ALS/PALSAR imagery: a D-InSAR geomorphological interpretation method. *Geomorphology* 231, 314–330. <https://doi.org/10.1016/j.geomorph.2014.11.031>.
- Shi, S., Zhang, F., Feng, D., Tang, K.W., 2020. Creep Constitutive Model for Frozen Soils Based on Hardening and Damage Effects. *KSCE J. Civ. Eng.* 24, 1146–1158. <https://doi.org/10.1007/s12205-020-1681-y>.
- Song, C.Q., Huang, B., Richards, K., Ke, L.H., Hien Phan, V., 2014. Accelerated Lake expansion on the Tibetan Plateau in the 2000s: Induced by glacial melting or other processes? *Water Resources Res.* 50, 3170–3186. <https://doi.org/10.1002/2013WR014724>.
- Sun, J., Qin, X., Yang, J., 2015. The response of vegetation dynamics of the different alpine grassland types to temperature and precipitation on the Tibetan Plateau. *Environ. Monit. Assess.* 188, 1–11. <https://doi.org/10.1007/s10661-015-5014-4>.
- Sun, Z., Wang, Y.B., Sun, Y., Niu, F.J., Guo, Y.L., Gao, Z.Y., 2017. Creep characteristics and process analyses of a thaw slump in the permafrost region of the Qinghai-Tibet Plateau, China. *Geomorphology* 293, 1–10. <https://doi.org/10.1016/j.geomorph.2017.04.045>.
- Tong, X.P., David, S., 2016. Active movement of the Cascade landslide complex in Washington from a coherence-based InSAR time series method. *Remote Sens. Environ.* 186, 405–415. <https://doi.org/10.1016/j.rse.2016.09.008>.
- Wasowski, J., Bovenga, F., 2014. Investigating landslides and unstable slopes with satellite multi-temporal interferometry: current issues and future perspectives. *Eng. Geol.* 174, 103–138. <https://doi.org/10.1016/j.enggeo.2014.03.003>.
- Wasowski, J., Bovenga, F., Dijkstra, T., Meng, X., Nutricat, R., Chiaradia, M.T., 2014. Persistent scatterers interferometry provides insight on slope deformations and landslide activity in the mountains of Zhouqu, Gansu, China. *Springer International Publishing* 19, 359–364. https://doi.org/10.1007/978-3-319-05050-8_56.
- Wu, T.H., Zhao, L., Li, R., Wang, Q.X., Xie, C.W., Pang, Q.Q., 2013. Recent ground surface warming and its effects on permafrost on the central Qinghai-Tibet Plateau. *Int. J. Climatol.* 33, 920–930. <https://doi.org/10.1002/joc.3479>.
- Xu, B., Li, Z.W., Wang, Q.J., Jiang, M., Zhu, J.J., Ding, X.L., 2013. A refined strategy for removing composite errors of SAR interferogram. *IEEE Geosci. Remote Sens. Lett.* 11, 143–147. <https://doi.org/10.1109/LGRS.2013.2250903>.
- Yang, Y., Wu, Q., Jiang, G., Zhang, P., 2017. Stable isotopic stratification and growth patterns of ground ice in permafrost on the Qinghai-Tibet Plateau, China. *Permafrost and Periglacial Processes*. 28, 119–129. <https://doi.org/10.1002/ppp.1892>.
- Yin, G.A., Luo, J., Niu, F.J., Lin, Z.J., Liu, M.H., 2021. Machine learning-based thermokarst landslide susceptibility modeling across the permafrost region on the Qinghai-Tibet Plateau. *Landslides* 112, 1–11. <https://doi.org/10.1016/j.cageo.2017.11.019>.
- Yu, Y., Guo, B., Wang, C.L., Zang, W.Q., Huang, X.Z., Wu, Z.W., Xu, M., Zhou, K.D., Li, J. L., Yang, Y., 2023. Carbon storage simulation and analysis in Beijing-Tianjin-Hebei region based on CA-plus model under dual-carbon background. *Geomat. Nat. Haz. Risk* 14, 1–23. <https://doi.org/10.1080/19475705.2023.2173661>.
- Zhang, Y., Meng, X.M., Chen, G., Qiao, L., Zeng, R., Chang, J., 2016. Detection of geohazards in the Bailong River Basin using synthetic aperture radar interferometry. *Landslides* 13, 1273–1284. <https://doi.org/10.1007/s10346-015-0660-8>.
- Zhang, Y., Meng, X., Jordan, C., Novellino, A., Dijkstra, T., Chen, G., 2018. Investigating slow-moving landslides in the Zhouqu region of China using InSAR time series. *Landslides* 15, 1299–1315. <https://doi.org/10.1007/s10346-018-0954-8>.
- Zhang, X.F., Zhang, H., Wang, C., Tang, Y., Zhang, B., Wu, F., 2019. Time-Series InSAR Monitoring of Permafrost Freeze-Thaw Seasonal Displacement over Qinghai-Tibetan Plateau Using Sentinel-1 Data. *Remote Sens. (Basel)* 11, 1000–1018. <https://doi.org/10.3390/rs11091000>.
- Zhao, R., Li, Z.W., Feng, G.C., Wang, Q.J., Hu, J., 2016. Monitoring surface deformation over permafrost with an improved SBAS-InSAR algorithm: with emphasis on climatic factors modeling. *Remote Sens. Environ.* 184, 276–287. <https://doi.org/10.1016/j.rse.2016.07.019>.
- Zheng, Z., Xie, C., He, Y., Zhu, M., Huang, W., Shao, T., 2022. Monitoring Potential Geological Hazards with Different InSAR Algorithms. The Case of Western Sichuan. *Remote Sensing*. 14, 2049. <https://doi.org/10.3390/rs14092049>.
- Zhou, C., Cao, Y., Yin, K., Wang, Y., Shi, X., Catani, F., Ahmed, B., 2020. Landslide Characterization Applying Sentinel-1 Images and InSAR Technique. The Muyubao Landslide in the Three Gorges Reservoir Area. China. *Remote Sens.* 12, 3385. <https://doi.org/10.3390/rs12203385>.
- Zhou, J., Zhang, X., Tang, W., Ding, L., Ma, J., Zhang, X., 2021. Daily 1-km all-weather land surface temperature dataset for the Chinese landmass and its surrounding areas (TRIMS LST; 2000–2021). National Tibetan Plateau/Third Pole Environment Data Center. <https://doi.org/10.11888/Meteoro.tpd.271252>. CSTR: 18406.11. Meteoro. tpd.271252.
- Zwieback, S., Kokelj, S.V., Günther, F., Boike, J., Grosse, G., Hajnsek, I., 2017. Subseasonal thaw slump mass wasting is not consistently energy limited at the landscape scale. *Cryosphere Discuss.* 12, 1–24. <https://doi.org/10.5194/tc-12-549-2018>.